Numerical simulation of tropical cumulus congestus during TOGA COARE

by D. B. Mechem and A. J. Oberthaler

2013

Numerical simulation of tropical cumulus congestus during TOGA COARE

D. B. Mechem[1] and A. J. Oberthaler[1,2]

Received 5 September 2012; revised 18 June 2013; accepted 10 July 2013; published 17 September 2013.

[1] Recent observational studies of tropical deep convection typically include some mention of cumulus congestus, a third mode of tropical convection, in addition to shallow trade cumulus and deep convection. This study analyzes congestus behavior in a multiday cloud-resolving model simulation based on the Tropical Ocean-Global Atmosphere Coupled Ocean-Atmosphere Response Experiment (TOGA COARE) field campaign. Simulation results exhibit a pronounced congestus cloud mode, present during both suppressed and active phases of the intraseasonal oscillation (ISO), with a unique signature consistent with cloudy-air detrainment near the 0°C isotherm. Congestus clouds in the simulation contribute 34% of the total precipitation during a 10 day transition period from suppressed to active phases, a number which corresponds well with previous estimates of the congestus contribution to precipitation. Domain-mean profiles and statistics from conditionally sampled buoyant cloud cores are compared with similar quantities from a recent model intercomparison of RICO trade cumulus. In many respects, cumulus congestus act like overgrown trade cumulus clouds. Both cloud types demonstrate multiple cloud fraction maxima associated with cloud base and detrainment layers. Profiles of buoyancy flux and vertical velocity variance suggest that the buoyancy production of turbulence behaves similarly in both cloud types. The greater precipitation production in the simulated congestus clouds nearly balances the surface latent heat flux, and thus the congestus contribution to moistening the atmosphere is limited. The computational configuration is a compromise between providing both sufficient resolution to represent shallow cumulus and sufficient domain size to handle broader, deep convective clouds.

Citation: Mechem, D. B., and A. J. Oberthaler (2013), Numerical simulation of tropical cumulus congestus during TOGA COARE, *J. Adv. Model. Earth Syst.*, *5*, 623–637, doi:10.1002/jame.20043.

1. Introduction

[2] Tropical convection has long been recognized as exhibiting two distinct modes: shallow trade cumulus, which range in depth from 2 to 3 km; and deep convection, which potentially extends up to the tropical tropopause. Studies as far back as *Malkus* [1962] and *Malkus and Riehl* [1964] have acknowledged the existence of a third mode of tropical cloudiness, that of cumulus congestus. *Simpson et al*. [1982] (formerly Malkus) went so far as to conduct an early numerical study of GATE (Global Atmospheric Research Program's Atlantic Tropical Experiment) congestus, predominantly emphasizing the roles of entrainment and detrainment. Perhaps the most single-purposed research thrust into the topic of cumulus congestus was the work of *Johnson et al*. [1999], who employed ship-board radar data from the Tropical Ocean—Global Atmosphere Coupled Ocean-—Atmosphere Response Experiment (TOGA COARE) field campaign to demonstrate robustly this third mode of tropical cloudiness (congestus) in vertical profiles of divergence, detrainment, and fractional cloudiness.

[3] Surface-based millimeter-wave cloud radar studies have confirmed the prevalence of congestus [*Hollars et al*., 2004; *Jensen and Del Genio*, 2006; *Stephens and Wood*, 2007], and cumulus congestus have been identified by space-based radar as well. *Casey et al*. [2007] found that midlevel clouds constitute a fractional areal coverage of 11.5% and a precipitating cloud fraction of 6.5%. In their study of shallow precipitation over the tropical oceans using data from the Tropical Rainfall Measuring Mission (TRMM), *Short and Nakamura* [2008] found a shallow mode of cloudiness in the range of 2–3 km and an upper congestus mode near 5 km. The shallow cumulus mode was present during nearly all periods of suppressed and active convection.

[1]Atmospheric Science Program, Department of Geography, University of Kansas, Lawrence, Kansas, USA.
[2]Department of Meteorology, Pennsylvania State University, State College, Pennsylvania, USA.

1942-2466/13/10.1002/jame.20043

Increasing rainfall was accompanied by an increase in the prevalence of the 5 km congestus mode. *Schumacher and Houze* [2003] found substantial amounts of "shallow, isolated rain," warm clouds they classified as congestus or isolated (presumably shallow) cumulonimbus. Using data from the CloudSat cloud profiling radar (CPR), *Luo et al*. [2009] identified congestus but cautioned that instantaneous snapshots of echo-top heights may instead capture clouds in their growing (transient) stages on the way to becoming deep cumulonimbus, suggesting that care is warranted when interpreting statistics based on uncorrelated, instantaneous snapshot fields. Sophisticated multisensor approaches have been developed to identify marine congestus clouds more accurately [*Casey et al*., 2012].

[4] The prevalence of cumulus congestus has suggested they may be an important source of tropical precipitation. *Cheng and Houze* [1979] found that 30% of the tropical rainfall in GATE fell from clouds with echo tops from 4 to 9 km. (This estimate comes from *Johnson et al*. [1999], who obtain it from Figure 2 in *Cheng and Houze* [1979].) *Johnson et al*. [1999] found that congestus clouds (defined by radar echo-top heights ranging from 4.5 to 9.5 km) contributed 28% of the rainfall during the TOGA-COARE field campaign. Employing a comprehensive classification scheme that took into account multilayered clouds, *Stephens and Wood* [2007] found a cloud mode centered at 5 km that gave precipitation contributions of 27.3% (obtained from the sum of Classes B and E, both single and multilayered, corresponding in their Table 3 to the transition phase of the intraseasonal oscillation (ISO) over the Atmospheric Radiation Measurement Program Tropical Western Pacific (ARM–TWP) Manus site). Radar-derived precipitation retrievals from TRMM reveal that warm clouds contribute 20% of the tropical maritime rainfall, although approximately half of these clouds are adjacent to deeper precipitating systems [*Liu and Zipser*, 2009].

[5] These previous studies have identified cloud top using a wide variety of reflectivity thresholds that generally depend on the sensitivity of the radar employed. Employing the ship-based radar from TOGA COARE placed aboard the R/V Vickers (the minimum interference threshold (MIT) radar, also used by *Johnson et al*. [1999]), *DeMott and Rutledge* [1998] defined echo-top as the height of the 0 dB Z level, although the actual sensitivity may have been higher (i.e., better) than this [see *Short et al*., 1997, Figure 3]. By way of comparison, the sensitivity of the TRMM precipitation radar used by *Short and Nakamura* [2008] was 18 dB Z. High-frequency cloud radars used to detect echo-top height have greater sensitivity. For example, the CloudSat CPR, employed in a number of studies that noted or explicitly addressed congestus [*Haynes and Stephens*, 2007; *Mace et al*., 2007; *Zhang et al*., 2007; *Luo et al*., 2009; *Casey et al*., 2012], had a sensitivity of -30 dB Z [*Tanelli et al*., 2008], whereas the Atmospheric Radiation Measurement Program 35 GHz millimeter-wave cloud radar employed in *Jensen and Del Genio* [2006] had a sensitivity between -30 and -47, depending upon the scanning mode [*Clothiaux et al*., 1995]. These differences in radar characteristics may produce substantial study-to-study differences in echo-top identification.

[6] The vertical extent of congestus clouds is thought to be tied to a weakly stable layer corresponding to intrusions of warm, dry air in the midtroposphere from the midlatitudes [*Yoneyama and Parsons*, 1999]. These layers of dry air were a robust feature during TOGA COARE [*Johnson et al*., 1996; *Mapes and Zuidema*, 1996; *Brown and Zhang*, 1997] and have been identified using longer term in situ [*Jensen and Del Genio*, 2006; *Takemi et al*., 2004] and remotely sensed [*Casey et al*., 2009] observations. *Mapes and Zuidema* [1996] concluded that the dry layers are radiatively active in the sense that the interaction of longwave radiative fluxes with the vertical humidity structure strongly influences the thermal structure. Thus, the anomalously warm, dry stable layers are an impediment to vertical cloud development, an effect that has been reproduced in numerical simulations [*Redelsperger et al*., 2002].

[7] The role of cumulus congestus in the large-scale tropical circulation is not well understood. Detraining congestus clouds serve to moisten and destabilize the dry stable layer [*Waite and Khouider*, 2010] in a manner similar to how shallow cumulus interact with the trade inversion [*Riehl et al*., 1951; *Betts*, 1973; *Stevens*, 2007]. This moistening and destabilization may serve to precondition the tropical atmosphere for deep convection. Furthermore, simulations have demonstrated that the best representation of the MJO (Madden-Julian Oscillation, which, for the purposes of this paper, we use interchangeably with ISO) [*Madden and Julian*, 1971, 1972] wave structure is associated with a bottom-heavy latent heating profile [*Li et al*., 2009]. A bottom-heavy diabatic heating profile would be consistent with a sizable contribution to surface precipitation from congestus clouds.

[8] Previous numerical simulation studies of congestus have addressed either dynamical [*Simpson et al*., 1982; *Carpenter et al*., 1998a, 1998b, 1998c] or microphysical [*Kogan*, 1991; *Lasher-Trapp et al*., 2001] aspects of individual cumulus congestus clouds, but relatively few studies [*Redelsperger et al*., 2002; *Waite and Khouider*, 2010] (discussed above) have explored the behavior of an ensemble of congestus clouds. In this research, we explore the behavior of cumulus congestus clouds as part of the large-scale tropical wave structure (specifically, the MJO) through high-resolution, multiday simulations that span the time period of the MJO as it transitions from the suppressed phase into a more active period of organized deep convection. In particular, we are interested in the joint behavior of shallow, congestus, and deep convection; the contribution of congestus to tropical precipitation; and the comparison of congestus characteristics with recent simulations of shallow trade cumulus clouds.

2. Model Description

[9] We employ the System for Atmospheric Modeling (SAM version 6.7.4 [*Khairoutdinov and Randall*, 2003]).

The conservation equations in SAM are based on anelastic dynamics, and scalar advection is formulated using a scheme that is both positive-definite and monotonic [*Smolarkiewicz and Grabowski*, 1990]. The model uses liquid/ice moist static energy for its prognostic thermodynamic variable. A Rayleigh damping layer is applied at grid points above 21 km.

[10] The ice-phase microphysical parameterization is loosely based on the approach of *Lin et al*. [1983] and *Rutledge and Hobbs* [1984], as outlined in *Khairoutdinov and Randall* [2003]. The model solves two conservation equations for water, one for total precipitating species (rain, snow, and graupel) and one for nonprecipitating quantities (vapor, cloud water, and cloud ice). The method of *Deardorff* [1980] parameterizes subgrid-scale (SGS) transports. As in *Khairoutdinov and Randall* [2003], the SGS mixing length in the *Deardorff* closure has been modified to equal the local vertical grid length. The parameterization for shortwave and longwave radiation is taken from the NCAR Community Atmospheric Model (CAM3) [*Collins et al*., 2006].

[11] All simulations are three-dimensional and employ a horizontal grid spacing of 200 m and doubly periodic lateral boundary conditions. *Bryan et al*. [2003] demonstrated that grid spacings of O(∼100 m) are required in order to adequately represent the inertial subrange in a simulated squall line. In our simulations, a grid spacing of 200 m is a compromise between being able to resolve turbulent fluxes associated with shallow cumulus and congestus, and the need for a domain large enough to represent the development of mesoscale organization associated with both shallow and deep convection. Recent studies have demonstrated that grid sizes of this magnitude do a respectable job of simulating boundary-layer clouds [*Wang and Feingold*, 2009a, 2009b; *Mechem et al*., 2012]. The number of grid points is $512 \times 128 \times 165$ for a domain size of $102.2 \times 25.4 \times 29.8$ km^3. The rectangular domain configuration was chosen under the assumption that a longer west-east extent would accommodate a greater degree of mesoscale organization relative to a square domain of a similar number of points.

[12] The simulations employ a stretched vertical grid, which ranges in spacing from 50 m at the surface to ∼600 m at 20 km. The grid configuration is plotted in Figure 1, overlaid with what *Khairoutdinov et al*. [2009] term a typical SAM vertical grid ("nz = 96"), along with the grid used for their high-resolution simulations. *Khairoutdinov et al*. [2009] found that fine vertical grid spacing was a requirement for adequately representing cumulus congestus. With this in mind, from the surface to 7 km, we employ a vertical grid ranging from 50 to 100 m, as in Figure 1.

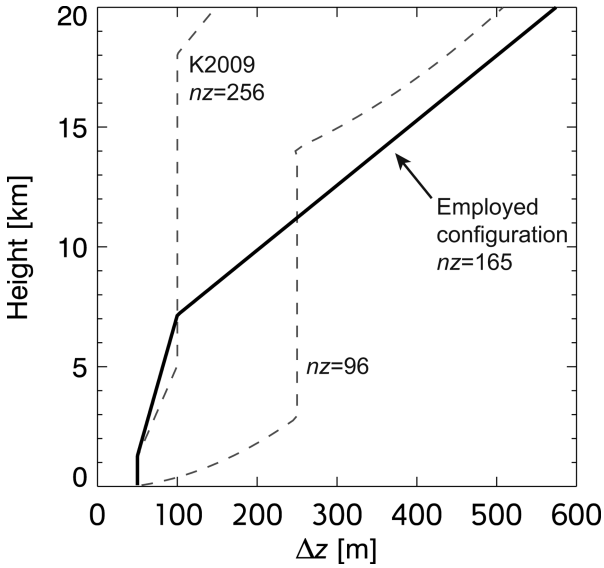

Figure 1. Vertical grid as a function of height for three different grid configurations. The number of vertical grid points in each configuration is noted on the figure.

3. Simulation Methodology

[13] The simulations employ the commonly used semidiagnostic framework where cloud properties evolve according to cloud-scale and mesoscale dynamics that respond to observationally constrained budgets of temperature and moisture [e.g., *Wu et al*., 1998; *Zeng et al*., 2009]. The semidiagnostic approach assumes a separation of scales and a one-way (downscale) interaction in which cloud systems respond to an imposed large-scale forcing. Thus, the cloud scale and large scale are not truly interactive. The large-scale forcing associated with convectively coupled tropical waves is presumed to contain transports of heat, moisture, and momentum arising from the observed cloud ensembles. In this simulation framework, the large-scale forcing (as well as any nudging to the large-scale fields) to some degree limits the upscale influence of the cloud transports to the large scale. Nevertheless, from the cloud behavior, we may infer feedbacks onto the large scale.

[14] Initial and boundary conditions were calculated from the TOGA COARE [*Webster and Lukas*, 1993] field observations using the variational method of *Zhang and Lin* [1997], who performed the processing. The analysis yields characteristic vertical profiles, time tendencies, and large-scale vertical motion valid over the TOGA COARE Intensive Flux Array (IFA, roughly centered at 155°E longitude, 2°S latitude; see Figure 14 in *Webster and Lukas* [1993]). The 20 day simulations begin at 0000 UTC on 25 November (day 330) and run until 0000 UTC on 15 December (day 350). Most of this period coincides with the suppressed phase of the intraseasonal oscillation (ISO), when organized deep convection over the IFA was rare [*Chen et al*., 1996]. Roughly speaking, the period corresponds to the range of Phase 3 to Phase 6 in the MJO classification index of *Wheeler and Hendon* [2004]. The middle of December marks the transition from suppressed to active phase of the ISO. Our model analysis focuses on a window centered on this transition period, ranging from 5 to 15 December, in order to emphasize the behavior of cumulus congestus clouds before, during, and after the transition to the organized deep convective regime.

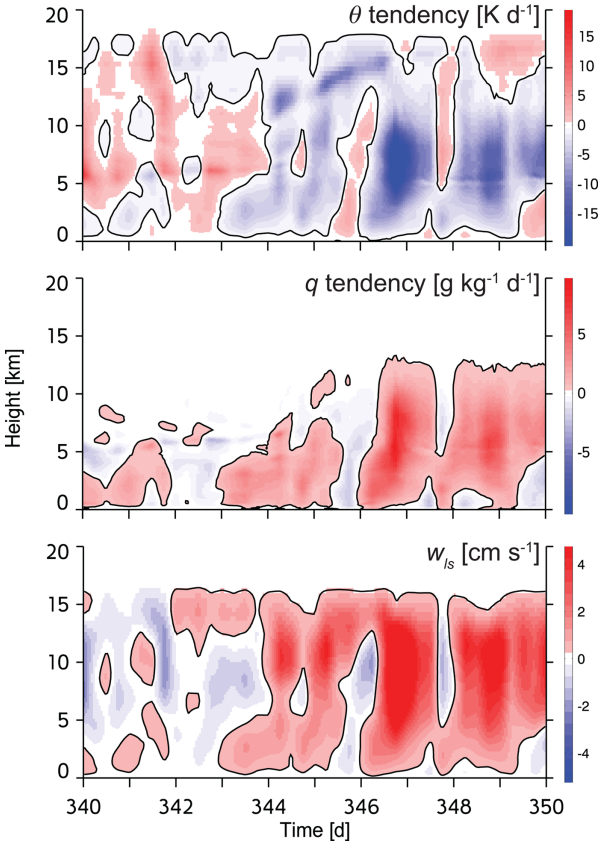

Figure 2. Time-height representation of large-scale forcing tendencies (potential temperature and moisture tendencies, and large-scale vertical velocity) applied to the model fields over the last 10 days of the simulation.

[15] Figure 2 shows the large-scale forcing corresponding to the last 10 days of the simulation. From days 340 to 344, the q tendency (corresponding to large-scale moisture advection) is confined to below the 6 km level, and after day 344, the tendency becomes more positive and deeper. This behavior is associated with the transition from the suppressed to the active phase of the ISO. The large-scale temperature tendency is largely a warming in the suppressed phase and cooling in the active phase. Both the θ (potential temperature) and q tendencies are synchronized with the large-scale vertical motion field w_{ls}. Warming and drying accompanies subsidence; cooling and moistening accompanies upward vertical motion.

[16] The model u and v winds are nudged to values specified by the variational analysis, with a timescale of 2 h. The evolving surface scalar fluxes are fixed and specified from the variational analysis. The surface stress (momentum flux) evolves interactively, under the assumption of a roughness length of 1.0×10^{-4} m.

4. Control Simulation Summary

[17] The simulation follows the prescribed forcing in Figure 2. The suppressed period from days 340 to 343 is characterized by shallow cumulus and cumulus congestus clouds (Figure 3). These cloud-top heights correspond to the highest vertical model grid point where the precipitating hydrometeor threshold (q_p) exceeds 0.001 g kg^{-1}. Thus, this method of identification corresponds more to a radar echo top than to actual cloud, but the approach is consistent with radar-based observational studies, such as those by *Cheng and Houze* [1979] and *Johnson et al.* [1999]. The 0.001 g kg^{-1} threshold corresponds to -12 dB Z (calculation based on *Ferrier* [1994], assuming liquid phase only), which corresponds to drizzle-sized droplets but lies below the sensitivity of most precipitation radars.

[18] From Figure 3, it is evident that shallow cumulus (defined here as cloud-top heights <3 km) are small in horizontal extent but numerous in number. A fewer number of deeper cumulus congestus clouds extend in height up to ~7 km. The congestus clouds are larger in size, suggesting they exhibit less dilution of their buoyancy via entrainment than their shallower counterparts.

[19] The transition from the suppressed to active phases of the ISO is characterized by convection that is deeper and more organized. The relatively small domain in our simulations ultimately limits the degree of mesoscale organization possible. We note that even at times when much of the domain is covered by cloud (e.g., day 348), the area fraction of cloudy buoyant updraft cores remains rather small (<0.12). From day 344 to day 349, cloud tops reach above 15 km, although at some times (day 347), deep convective activity is limited. Shallow cumulus and congestus are present during these times between deep convective events. Even when deep convection is widespread (e.g., day 349), Figure 3 indicates that shallow cumulus and congestus are visible in the regions outside of active deep convection. This coexisting nature of congestus and deep convection will be more evident when we consider the vertical structure of the precipitating systems.

[20] The transition from suppressed to active phases of the ISO is evident in Figure 4, which shows vertical profiles of horizontally averaged cloud particles (q_c, which includes both nonprecipitating cloud water and cloud ice) and precipitation (q_p, which includes rain, snow, and graupel). During the suppressed period from days 340 to 344, cloud tops are limited to <7 km. The peak in q_c at ~2 km corresponds to the shallow trade cumulus mode. A secondary maximum near the cloud top at ~5 km corresponds to cumulus congestus likely detraining at a layer of enhanced stability roughly associated with the 0°C temperature level. In short-term simulations of tropical convection, *Khairoutdinov et al.* [2009] also found evidence of this congestus behavior intermingled with deep convection. They also found that whether or not the model produced these clouds was acutely dependent upon using a fine vertical grid spacing. We found a similar sensitivity using the "nz = 96" vertical grid in Figure 1, with some slight differences. Strangely enough, when running with insufficient vertical resolution, midlevel clouds were nevertheless present and the model was able to capture the congestus mode in the precipitation field. However, the detrainment maximum in q_c near the 0°C level was

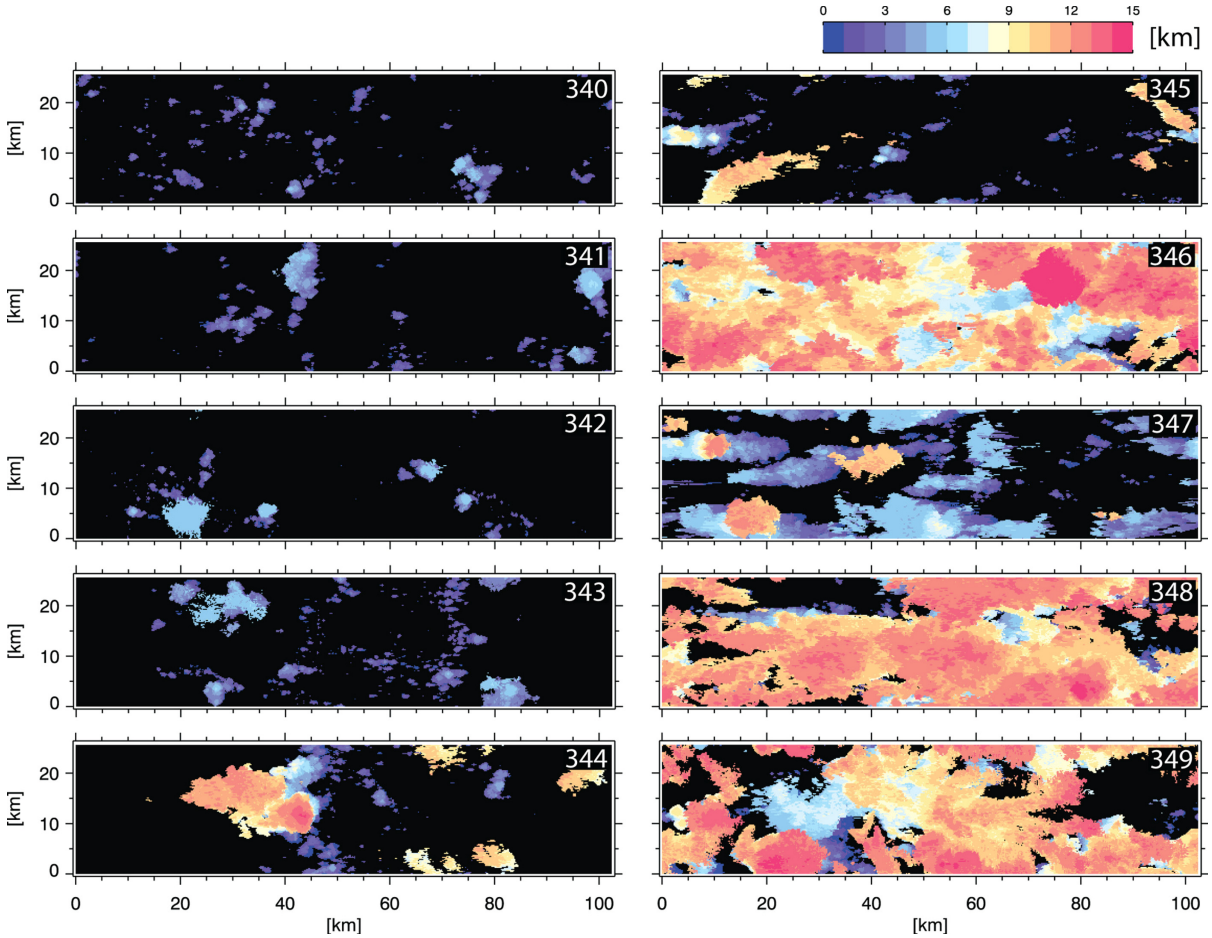

Figure 3. Daily sequence of echo-top heights at 0000 UTC, calculated from the simulation output. The calculation methodology is described in the body of the text.

only weakly present. The vertically continuous extent of the mean profiles of precipitation hydrometeors (q_p) in Figure 4 (i.e., the lack of multiple maxima) suggests that the fewer number of clouds reaching up to the 5–7 km altitude may contribute similar amounts of precipitation as the greater number of low clouds. In section 5, we analyze the relative contributions of cloud depth on precipitation.

[21] The active period (from 344.5 to350 h) also contains evidence of cloud-top detrainment associated with congestus, particularly evident from days 347 to 350. This is not a radar bright band feature, though it is visually similar. Time periods between periods of organized convection (e.g., day 348) exhibit similar behavior to the suppressed period, with shallow cumulus and congestus present. The simulation behavior is consistent with the view of *Short and Nakamura* [2008], indicating that shallow convection is nearly always present in the tropics, even when deep convection is active.

[22] The precipitation mixing ratio field ($q_p = q_r + q_s + q_g$, a sum of rain water, snow, and graupel mixing ratios) reflects the connection between clouds of various depths and the amount of precipitation. Some amount of surface precipitation is always present, and deeper clouds tend to rain more. Even during the suppressed period from 340 to 344.5, the deeper clouds produce more precipitation. Larger values of q_p in Figure 4 tend to accompany the appearance of detrainment in q_c (e.g., 343–344).

5. Contribution of Congestus to Precipitation

[23] The mean profiles of q_c and q_p in Figure 4 are consistent with the relationship between rain rate and cloud depth. However, at any given time, a distribution of cloud depths may be present, each potentially contributing to the surface rainfall. Ultimately, we seek the contribution to surface rainfall from clouds of all different heights. The evolution of model-derived echo-top height is shown in Figure 5 and is a compact way of looking at the temporal evolution of echo-top distributions from fields like those shown in Figure 3. As previously noted, this "echo-top height" calculation is based on the maximum height where precipitation mixing ratio exceeds a specific threshold (1.0×10^{-3} g kg^{-1}). Thus, this quantity reflects the precipitation structure more than the cloud itself and facilitates comparison with radar-based studies [e.g., *Johnson et al.*, 1999].

[24] Histograms of echo-top height are calculated every 15 min, with a 1 km vertical bin size (Figure 5). The

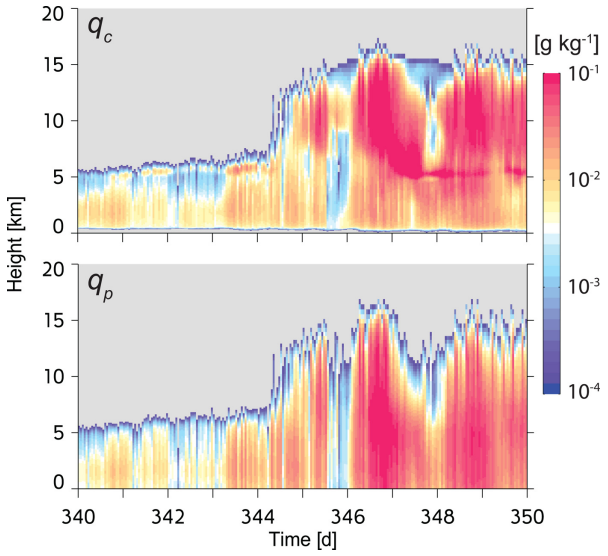

Figure 4. Time-height section of domain-mean cloud water mixing ratio (q_c) and precipitation mixing ratio (q_p).

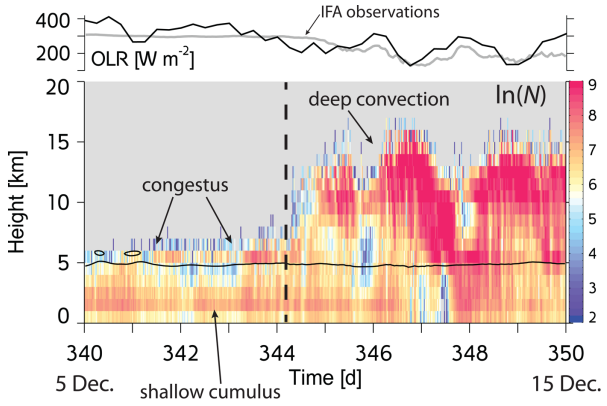

Figure 5. Time series of instantaneous histograms of echo-top height. The dashed line represents the transition from suppressed to active phase of the ISO. Shallow cumulus, congestus, and deep convective modes are indicated. The black line in the lower panel indicates the 0°C temperature level. Corresponding time series of outgoing longwave radiation from the simulation (black line) and from observational analysis (gray line) [*Ciesielski et al.*, 2003] are shown on the upper panel.

histograms represent the areal coverage of echo tops lying within a given bin. Immediately evident is the shallow cumulus mode, lying between 1 and 3 km. The shallow mode is nearly always present during the suppressed period, but it is also visible during the active phase, reflecting the explanation of *Short and Nakamura* [2008] that shallow cumulus is always "bubbling" in the tropical environment.

[25] Congestus are most evident in the suppressed period from days 340 to 344.5. The congestus mode is more transient than the shallow cumulus mode, but congestus nevertheless are frequently present. In the simulation, echo tops for congestus tend to lie most commonly in the 5–6 km range, though Figure 5 includes instances of congestus penetrating up to 7–8 km. The 0°C isotherm is associated with a stable layer [*Johnson et al.*, 1996], which the congestus updrafts are nevertheless able to penetrate (Figure 5). These congestus clouds, however, ascend no more than a kilometer or two above the 0°C isotherm.

[26] The assumptions of the microphysical parameterization in the model dictate that these clouds remain predominantly supercooled water, but this requirement is largely consistent with the lack of cold temperatures necessary for substantial ice-particle nucleation. Figure 5 indicates that the melting level is at or just below 5 km. The −5°C isotherm (not shown) hovers near 6 km during the suppressed phase and is topped by the midlevel temperature inversion. The temperatures at this level early in the period, while not unreasonable, are a few degrees warmer than the observations [*Ciesielski et al.*, 2003]. The physical reason for this warm bias is not clear, although the behavior is consistent with the potential temperature tendency between 5 and 7 km in Figure 2, which also promotes the temperature inversion in this layer.

[27] The decrease of temperatures in the midlevels is consistent with the melting and cooling that typically accompanies stratiform precipitation. Because ice nucleation is only weakly active at temperatures at and warmer than −5°C, we are confident that precipitation growth in congestus during the suppressed phase (days 340–344.5) is almost exclusively governed by collision-coalescence associated with the warm-rain process.

[28] Cloud system behavior is much more complicated following the transition to the deep convective phase (day 344.5). As mentioned, the shallow convection mode is still apparent. The short period from 344.5 to 350 nevertheless hints at pulses of deep convective activity on a 2 day period (see *Chen et al.* [1996] for a thorough summary of how this 2 day periodicity in convection is related to the large-scale dynamics in TOGA COARE). Echo tops corresponding to congestus (∼4–6 km) are present, but the existence of a distinct congestus mode is much less obvious than during the suppressed regime. Indeed, clouds of all different depths are present during the active phase.

[29] The time series of outgoing longwave radiation (OLR, Figure 5) calculated from the simulation is compared with the observed OLR over the IFA [*Ciesielski et al.*, 2003]. OLR is a good metric to ascertain the reasonableness of the simulated cloud distribution (good agreement would be considered a necessary, though not sufficient, condition for a reasonable cloud field), although by itself OLR is not sufficient to give much detail about the distribution itself. Over the 10 day simulation, agreement differs between simulation-derived OLR and the observations. Agreement is particularly good during the deep convective events during the second half of the period. Agreement during these times indicates the anvil temperature (altitude) is consistent with the observed convection. Between the strong

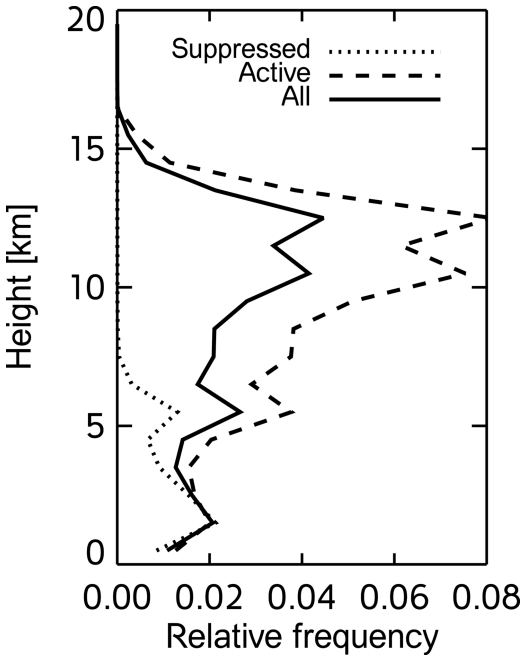

Figure 6. Relative frequency of echo-top height during suppressed and active phases, as described in the text. The suppressed phase is defined to be from 340 to 344.5 and the active phase from 344.5 to 350.

convective events, OLR differs between observations and model, with the model producing either lower clouds or lower cloud fraction (i.e., higher brightness temperature) than the observations. During the suppressed (early) phase, simulated OLR is, on average, substantially greater than observed (except for a short period near 0000 UTC on day 341). While this might be explained by an underestimate of congestus cloud fraction (greater radiating temperatures), we suspect the warm bias discussed above may play a role. Another possibility is the utter lack of deep convection during the suppressed period, when in reality, the suppressed period often contains instances of isolated deep convection [e.g., *Chen et al*., 1996, Figure 4a]. The lack of deep convective anvil in the simulations may then be a factor in overestimating the OLR, relative to the observations.

[30] Figure 6 summarizes the relative frequency of echo-top heights, stratified according to period. For example, a relative frequency of 0.027 at a height of 5.5 km means that, in the 5.0–5.5 km layer, 2.7% of the area is covered by echo tops residing in that layer. The calculation is a summary of Figure 5 rather than a statistic like the horizontally averaged fraction of q_p. The shallow cumulus mode is present during both the suppressed and active phases of the ISO. The congestus mode is also present during both periods. The areal coverage of congestus is substantially greater during the active phase, but both phases clearly exhibit the congestus mode. The deep convective mode is absent during the suppressed phase. This figure then demonstrates a continuum of echo-top height area but also the distinct presence of the TOGA COARE trimodal cloud structure documented by *Johnson et al*. [1999]. Although the simulation time does not fully correspond with any of the deployments of the MIT radar, the distributions may nevertheless be loosely compared with the convective cloud distributions from Figure 5 in *DeMott and Rutledge* [1998]. Compared to Figure 6, the DeMott and Rutledge distributions are more smoothly continuous, but they do hint at the congestus mode (particularly their Figure 5b). The maximum of their deep convective mode varies but tends to lie between 7 and 8 km, much lower than 10–12 km depth in our simulations. Our good OLR agreement between model and observations indicates the simulated cloud tops during deep convective events are reasonable, indicating the reflectivity associated with the q_p threshold in the model is too small, thus capturing too much low-reflectivity echo at high altitude.

[31] In order to better compare with the results of *Johnson et al*. [1999], we conducted a feature identification analysis using the North Carolina State University "blob" detection toolbox [*Miller and Yuter*, 2013]. The blob detection method employs accepted image processing algorithms for the identification of contiguous features. In order to identify individual cloud features for a specific time, we first calculate the column-maximum value of the three-dimensional precipitation water field (q_p), resulting in a two-dimensional array of column-maximum q_p. We then run the feature detection on this 2D field, which returns a number of connected regions we interpret as individual clouds. Echo-top height is then calculated from the median of echo-top heights (using the $q_p = 0.001$ g kg^{-1} threshold, as before) from all columns in the cloud feature. The detection operation is done for every instantaneous q_p field. One admitted drawback of this approach is that it is not able to identify shallow cumulus that are not precipitating.

[32] The cloud feature analysis shows either two or three distinct modes (Figure 7), depending on the phase of the ISO. The active phase contains more congestus features than does the suppressed phase, in addition to deep convective features, but it also contains fewer shallow clouds. The reason for this is not clear although may simply be a consequence of the limited domain size, with large areas of deep convection in the active phase leaving little room for shallow convection. This figure does allow comparison of the relative number of congestus and shallow clouds, which in *Johnson et al*. [1999] [their Figure 4] is constrained by assumptions based on prior observational campaigns. Throughout the 10 day simulation, the percentages of shallow and congestus cloud features are 68.3 and 15.2%. The cloud feature detection does a respectable job at identifying shallow and congestus clouds, but we feel it overestimates the number of independent, deep clouds. Clouds nearby deep convection, which should be considered as part of the deep convection feature, the software instead identifies as separate blobs. Judicious filtering of the input fields prior to running the feature detection would likely ameliorate this problem.

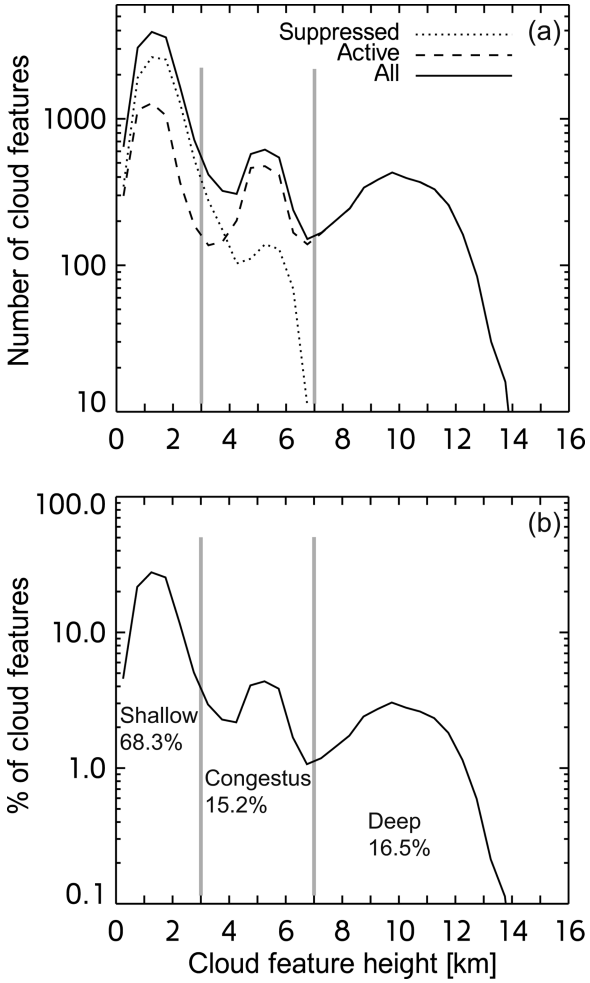

Figure 7. Frequency distributions of echo-top ("cloud feature") height. (a) Number of cloud features. (b) Relative frequency of cloud features. The y-axis represents the number or percentage of cloud features lying within 500 m of the specified altitude. Thick gray lines separate the shallow, congestus, and deep convective clouds by the criteria specified in the manuscript. Percentages represent the total fraction of cloud features lying within each regime.

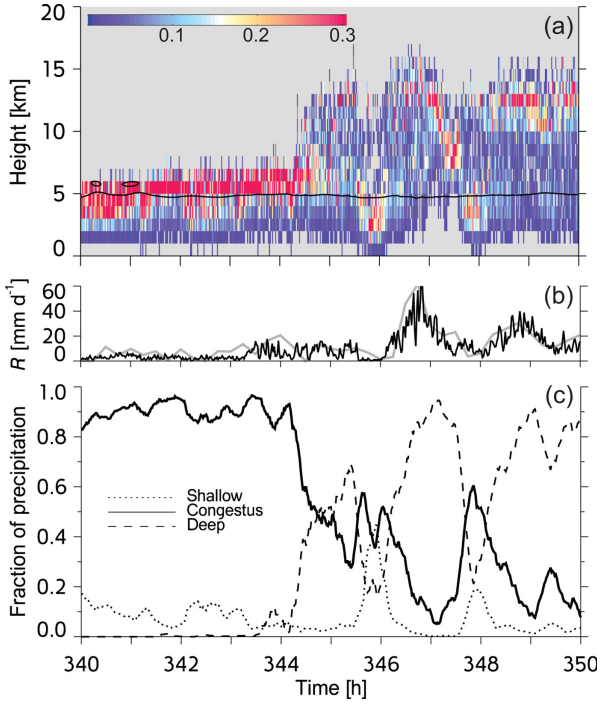

Figure 8. Time-height plot of fractional contribution to the total instantaneous precipitation rate. The contributions for any given time add up to 1.0 (100%). (b) Surface precipitation rate, with the gray line representing the observed TOGA COARE precipitation rate from *Ciesielski et al.* [2003]. (c) Fractional contribution for the three classes, as defined in the text.

[33] The relative contribution to the total precipitation from clouds of different depths varies substantially with time (Figure 8). The suppressed period (days 340–344.5) is characterized by a precipitation rate <5 mm d^{-1} from days 340 to 343.25, after which it increases (Figure 8b). The mean simulated precipitation rate agrees well with microwave-derived precipitation rates over the IFA for the period 5–15 December (both about 10 mm d^{-1} [see *Chen et al.*, 1996, Figure 4b]), although the simulated precipitation exhibits much larger instantaneous values (peak values of 60 mm d^{-1} versus 30 mm d^{-1} in *Chen et al.* [1996]). Agreement with precipitation rate estimated from the observational IFA budgets (from *Ciesielski et al.* [2003] overlaid on Figure 8b) is remarkable. The increase of precipitation during the suppressed phase is associated with the greater prevalence of congestus clouds, along with evidence of these clouds slowly deepening with time (Figure 4). The bulk of the precipitation during the suppressed phase is coming from congestus clouds (Figure 8a). During the active phase, clouds of all depths contribute to the surface precipitation.

[34] We further categorize the precipitation contribution in Fig. 8c into shallow, congestus, and deep clouds. Clouds are categorized as congestus if their echo-top height lies between 3 and 7 km (specifically 3 km $\leq z < 7$ km). This choice is somewhat arbitrary. The lower limit is justified based on an approximate upper limit of trade cumulus clouds; the upper bound is approximately 2 km above the 0° layer, a feature commonly associated with congestus clouds [*Johnson et al.*,1996,1999]. During the suppressed phase, the vast majority of the precipitation (80–95%) falls from congestus clouds (Figure 8c). Deep convective events contribute greatest to the strongest periods of precipitation during the active phase (e.g., days 347 and 349). However, some caveats are in order with respect to our simple cloud classification during the active phase. Shallower cumulus and congestus contribute to the precipitation during this period, too, although we suspect some of these contribution classified as congestus may represent precipitation falling from stratiform regions associated with mesoscale convective systems (MCSs), as opposed to originating from distinct, isolated congestus cells. Note, too,

Table 1. Contribution to Total Precipitation from Shallow Cumulus, Cumulus Congestus, and Deep Convection[a]

	Shallow (%)	Congestus (%)	Deep (%)	R (mm d^{-1})
Suppressed	5.2	87.0	7.8	4.1
Active	3.2	22.1	74.7	15.1
Entire period	3.6	34.0	62.4	10.1

[a]Precipitation contributions are calculated for the suppressed and active phases of the ISO, and for the entire period.

that the classification scheme does not fully take into account multilayer clouds. For example, congestus lying under a large cirrus cloud will be classified as deep convection. This miscategorization is likely occurring at 0000 UTC of day 349, where substantial cloud at 5 km (Fig. 4, upper panel) does not contribute substantially to the cloud distribution (Figure 5).

[35] The relative contributions from the three cloud types are summarized for the suppressed, active, and the entire period in Table 1. The ubiquitous shallow convection contributes less than about 5% of the surface precipitation, though shallow convection is important for the vertical transport of heat and moisture, and for maintaining the lower tropospheric vertical stratification against the large-scale subsidence. During the suppressed period, congestus clouds contribute 87% of the precipitation. The nonzero occurrence of deep convection arises because the transition from suppressed to active regime is gradual. During the active period, the bulk of the precipitation (74.7%) falls from the deep category; nevertheless, 22.1% of rainfall comes from congestus clouds. Calculated over the entire 10 day period spanning both suppressed and active periods, congestus clouds account for 34% of the precipitation. The contribution over the entire period is affected by the fractional contribution of the two constituent periods (suppressed and active phases), but the simulations suggest a lower bound to the total contribution should be at least 22.1%.

[36] These attributions of congestus precipitation are roughly consistent with *Cheng and Houze* [1979] [30%], *Johnson et al.* [1999] [28%], and *Stephens and Wood* [2007] [27.3%]. Our results are somewhat higher than the radiative-convective equilibrium simulations of *van den Heever et al.* [2011], who attribute 15.3–17.9% of tropical precipitation to congestus-type clouds (summarized from their Table 8, using their categories M1–M2 and M1–M2 and M3).

[37] Because of the overlapping nature of the cloud distribution (as opposed to three distinct modes), the contribution of congestus to the total precipitation is sensitive to the depth of clouds we consider congestus. Table 2 summarizes this sensitivity over the entire simulation period. For example, increasing the layer bounds of the congestus category from 3–7 km to 3–8 km increases the congestus contribution from 34.0 to 40.3%.

[38] Because our simulation does not span a complete period of the intraseasonal oscillation, the total contribution from congestus also depends on the lengths of the suppressed and active periods (with congestus being the dominant contribution to precipitation during the suppressed phase and deep convection being the main contributor during the active phase). Table 3 shows the congestus contribution during the active phase only, which represents a lower bound on the relative contribution to congestus clouds. The congestus contribution during the active phase is 22.1% (the 3–7 km layer), but this number is sensitive to the layer classification and the possibility that clouds classified as congestus are in reality stratiform rain component from MCSs.

Table 2. Amount of Congestus Precipitation as a Function of the Congestus Classification, Taken Over the Entire Simulation Period

	Layer Top (km)					
Layer Base (km)	5	6	7	8	9	10
2	15.8	29.0	36.8	43.1	48.3	54.2
3	13.1	25.2	34.0	40.3	45.5	51.4
4	7.5	19.6	28.4	34.7	39.9	45.8
5		12.2	21.9	27.3	32.5	38.3

6. Congestus as Overgrown Trade Cumulus

[39] The appearance of congestus suggests many similarities with trade cumulus. The idea that both shallow cumulus and congestus are governed predominantly by cumulus dynamics and warm-rain microphysical processes is a reasonable hypothesis. Congestus share many of the same characteristics with cumulus, only they are larger in both width and depth. Figure 9 shows tendencies in liquid water potential temperature ($\theta_l = \theta - \left(L_v/c_p\right)q_l$, where θ is potential temperature and q_l is liquid water mixing ratio) and total water (q_t, the sum of water vapor and all condensate) brought about by turbulent fluxes. These tendencies reflect the impact of only the turbulent fluxes and do not include the imposed large-scale forcing terms. During the suppressed period (days 340–344.5), the turbulent fluxes warm the boundary layer from the surface to ~2 km and cool above, particularly in the immediate vicinity of the layer where the congestus appear to detrain (5–6 km). A deep layer of moistening lies atop a shallow (0–2 km) layer of weak drying. The cooling-over-warming behavior is a signature of shallow convection [see *Stevens*, 2007, Figure 2], with surface fluxes acting to warm the lower part of the layer and adiabatically cooled

Table 3. Amount of Congestus Precipitation as a Function of the Congestus Classification, Taken Over the Active Phase Only

	Layer Top (km)					
Layer Base (km)	5	6	7	8	9	10
2	12.3	18.8	24.5	31.1	37.3	44.3
3	9.9	16.4	22.1	28.7	34.9	41.9
4	5.5	12.0	17.7	24.3	30.5	37.5
5		6.5	12.2	18.8	25.0	32.0

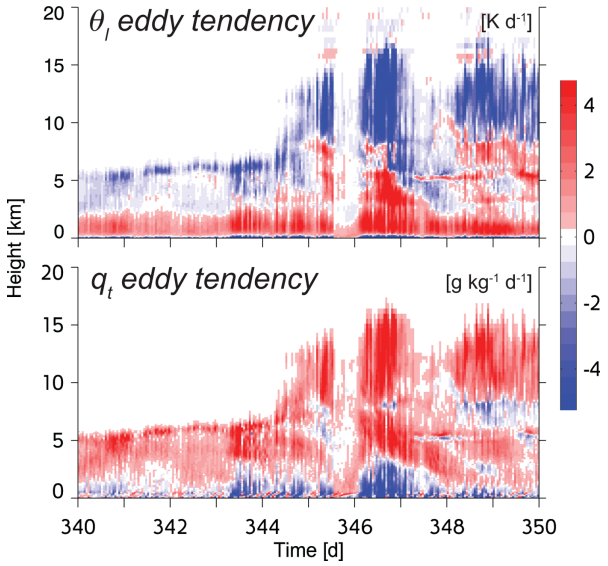

Figure 9. Time-height section of tendencies of liquid water potential temperature flux $\left[-\partial\left(\overline{w'\theta_l'}\right)/\partial z\right]$ and total water flux $\left[-\partial\left(\overline{w'q_t'}\right)/\partial z\right]$ from turbulent transports, with w denoting vertical velocity.

buoyant updrafts mixing with the warmer environment aloft associated with the trade inversion. Moisture increases with time over all depths in shallow cumulus [*Stevens*, 2007]. The shallow layer of drying below 2 km in Figure 9 accompanies congestus precipitation events and is likely associated with efficient removal of boundary-layer moisture and via vigorous congestus updrafts.

[40] Turbulent transports during the active phase are much more complicated, although much of the behavior of the 0–6 km layer remains similar. The most notable difference at low levels between the suppressed and active periods is the episode of drying on days 346–347, corresponding to the deep convective activity on that day. Figure 9 indicates cooling over much of the layer from 8 to 16 km. This pattern of cooling over warming in deep convective episodes is consistent with a series of SAM simulations of tropical deep convection by *Khairoutdinov and Randall* [2002]. The q_t tendency represents the ensemble effects of convection which act to dry the boundary layer and moisten the free troposphere, resulting in a column-net drying.

[41] Figure 10 contrasts the TOGA COARE mean vertical model profiles taken during the suppressed phase with trade cumulus profiles from RICO (Rain in Cumulus over the Ocean) [*Rauber et al.*, 2007]. The RICO trade cumulus profiles come from the trade cumulus intercomparison described in *van Zanten et al.* [2011] (specifically, the SAMEX simulation contributed by Mechem and Kogan). The two profiles could be normalized by depth according to, for example, cloud base and inversion heights (both the trade and 0°C inversions), but one gains more appreciation for the similarities and differences when viewing the profiles as a function of geometric height. The experimental setup for the two simulations differs substantially. The RICO simulation has finer resolution (100 and 40 m horizontal and vertical grid spacing, respectively) and a much more sophisticated treatment of microphysical processes (size-resolving "bin" microphysics).

[42] We note that the TOGA COARE profiles contain shallow cumulus present in the RICO simulation, in addition to the cumulus congestus clouds of interest. Both simulations contain a low-altitude maximum in cloud fraction associated with cloud base, and another relative maximum (2 km for RICO, 5.5 km for TOGA COARE) likely associated with cloud-top detrainment (Figure 10a). In both simulations, liquid water increases above cloud base to an altitude of ~2 km (Figure 10b). Above this layer, the RICO clouds lose all their buoyancy and completely detrain, whereas the TOGA COARE congestus continue ascending. The decrease of liquid water with height points to dilution via entrainment of the congestus updrafts. Precipitation is much greater in the TOGA COARE case (surface values of 4 versus 0.3 mm d^{-1}). Precipitation in RICO is maximum at 2 km, with evaporation contributing substantially to the decrease below this layer (Figure 10c). The TOGA COARE precipitation rate exhibits a similar maximum below 2 km, and the profile above this maximum is consistent with collision-coalescence of droplets falling through the layer from 7 km down to 2 km. Although a small amount of ice-phase microphysics is present in the model (largely an artifact of the simple microphysics parameterization, which partitions water between liquid and ice simply according to temperature), warm-rain microphysics governs the precipitation process. It is noteworthy that the relative magnitudes of the cloud (q_c) and precipitation (q_p) modes are similar in the TOGA COARE simulation (Figure 4), whereas in trade cumulus, the precipitation content is much smaller than the cloud water content (see Figure 8 in *van Zanten et al.* [2011] for profiles of the RICO trade cumulus simulations). This behavior perhaps speaks to the efficiency of the warm-rain process in the deeper congestus clouds, although this hypothesis would need to be evaluated in the TOGA COARE simulation with more sophisticated microphysical parameterizations.

[43] Both the RICO trade inversion and the inversion associated with the 0°C layer during TOGA COARE are evident in the static stability (Figure 10d). Recall from Figure 8 that the 0°C level is just below 5 km. The 0°C inversion is stronger than the trade inversion and is deeper. The stability evolves from both the large-scale forcing tendencies and the turbulent cloud transports.

[44] With the exception of different cloud depths, the liquid water potential temperature flux (Figure 10e) behaves quite similarly between the two cases. The θ_l fluxes in both cases imply a pattern of cooling-over-warming. The total water flux (Figure 10f) behaves very differently in the two simulations. In RICO, sedimentation flux (from precipitation) is only a minor portion of the total water budget, and most of the surface latent heat flux is applied toward moistening the deepening boundary layer. In the TOGA COARE simulation, on the other hand, precipitation is a substantial part of the

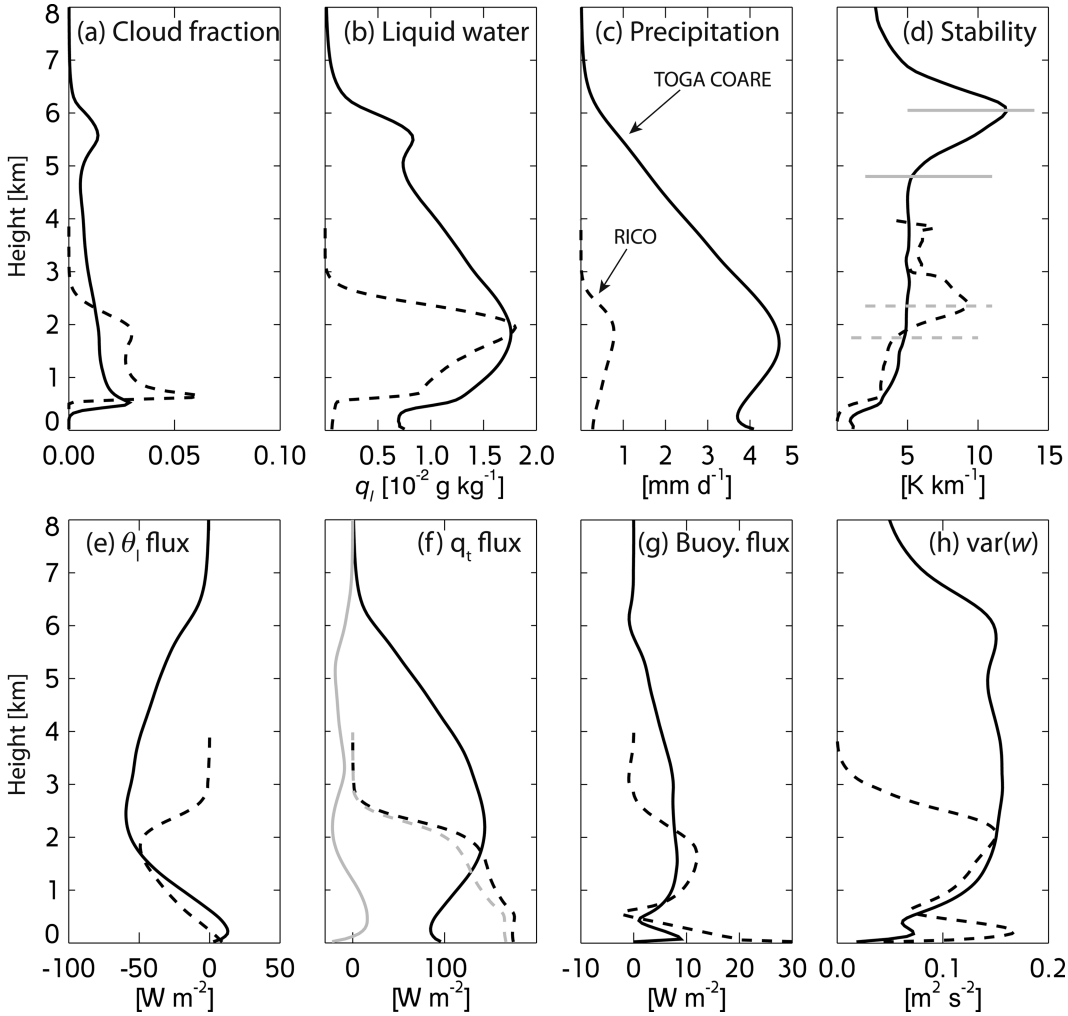

Figure 10. Mean profiles for the TOGA COARE (solid) and RICO (dashed) simulations calculated over the suppressed phase. (a) Cloud fraction f_c. (b) Liquid water q_l. (c) Precipitation rate R. (d) Dry static stability $d\theta/dz$. (e) Liquid water potential temperature flux $\rho c_p \overline{w'\theta_l'}$, where ρ is the air density and c_p is the specific heat at constant pressure. (f) Total water flux $\rho L_v \overline{w'q_t'}$, where L_v is the latent heat of vaporization. The gray lines include the sedimentation flux. (g) Buoyancy flux $\rho c_p \overline{w'\theta_v'}$. Note that the TOGA COARE simulation profile does not include the SGS contribution. (h) Vertical velocity variance $\overline{w'w'}$.

turbulent transports such that the net flux is near zero. The precipitation flux nearly balances out the latent heat flux, which means that the moistening of the troposphere is driven by any imposed large-scale moisture tendency.

[45] Buoyancy flux (Figure 10g) is very similar between the two simulations, with a minimum near cloud base and positive values in the cloud layer indicative of positively buoyant cloudy updrafts. This behavior of buoyancy generation of turbulence is reflected in the vertical velocity variance (Figure 10h), which shows a minimum associated with cloud base, sandwiched between maxima in the subcloud and cloud layer. These profiles reflect substantial similarities between trade cumulus and their deeper cousin, cumulus congestus.

[46] The profiles also display some substantial differences between the two cloud types. As previously discussed, the relatively greater importance of precipitation to the total water budget in congestus clouds suggests important microphysical differences associated with greater precipitation production. The greater precipitation rate in congestus (Figure 10c) is associated with much more efficient warm-rain processes. Deeper clouds have substantially great liquid water content (LWC), and it is well known (in shallow clouds, at least) that precipitation scales with LWC [*van Zanten et al.*, 2005] because of greater amounts of cloud droplets available for collection and drop growth. Conditionally sampled profiles discussed below show that congestus updrafts have larger values of LWC over a much greater depth relative to shallow cumulus.

[47] Mean profiles like those in Figure 10 serve to compare the area-mean properties and fluxes of the cloud field, which is related to the mean state and how it evolves with time. A detailed investigation of in-cloud behavior is beyond the scope of this work, but Figure 11

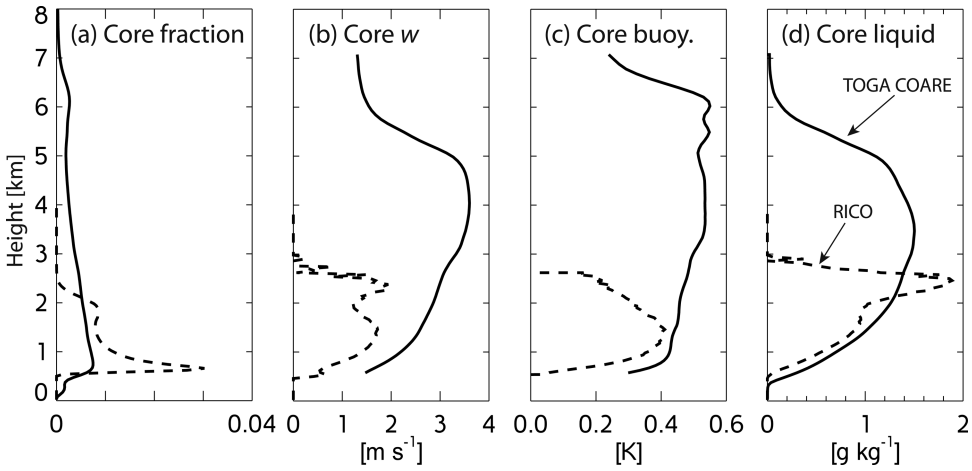

Figure 11. Mean properties of positively buoyant cloud cores for the TOGA COARE (solid) and RICO (dashed) simulations calculated over the suppressed phase. (a) Area fraction. (b) Vertical velocity. (c) Buoyancy excess (θ_v'). (d) Liquid water mixing ratio.

compares several properties associated with the clouds themselves. The profiles for Figure 11 are calculated by conditionally sampling these quantities over positively buoyant (composed largely of updrafts) cloudy points. Note that during the suppressed phase, the TOGA COARE profiles contain contributions from both shallow clouds and congestus. The TOGA COARE simulation does not contain the peak in core fraction (Figure 11a) associated with cloud base present in the RICO simulation. Given the prevalence of shallow cumulus in the tropics, we strongly suspect that the lack of this feature in the TOGA COARE simulation is an artifact of our choice of relatively crude grid spacing (200 m in the horizontal), which is insufficient to capture these small, shallow cloud features. Both core fraction profiles exhibit low-level maxima that decrease with height, which suggests entrainment reducing the convective core area. Convective core vertical motion (Figure 11b) during TOGA COARE is dominated by congestus, with values of w greater than those in RICO. Buoyancy excess ($\theta_v' = \theta_v - \overline{\theta_v}$, Figure 11c) differs between the simulations and in the TOGA COARE maintains a value of $\sim$0.5 K from 3.5 km up to 6 km. This result, together with the core fraction decreasing with height, suggests one interpretation where the number of cores decrease with height but that the cores that remain are able to maintain their buoyancy. The behavior of core liquid water is similar in the two simulations (Figure 11d), differing only in depth and the presence of a liquid water maximum in the upper part of the RICO profile.

7. Discussion and Conclusions

[48] The ultimate contribution of congestus clouds depends upon how congestus are defined. We have attempted to mimic roughly the cloud categories of *Johnson et al.* [1999], but we also find that the contribution to surface precipitation is sensitive to how the categories are defined. For example, *Short and Nakamura* [2008] find that shallow cumulus contribute $\sim$21% of tropical rainfall but only 5% of rainfall in convectively active regions. Furthermore, because of their analysis methodology, it appears that their upper mode at 5 km includes contributions from both congestus and deep, organized cumulonimbus. The lower height limit for congestus can be tied to the trade inversion, but because the congestus inversion is more diffuse or sometimes absent altogether, no clear choice exists for how to define the upper bound for congestus clouds. The choice of upper bound should be made to capture as much of the congestus mode as possible while minimizing the aliasing of deep convection into the congestus category.

[49] Our conclusions are as follows:

[50] 1. We find that congestus clouds contribute 34% of the precipitation in our 10 day analysis period of TOGA COARE convection, a number that is in reasonable agreement with previous observational studies of tropical deep convection.

[51] 2.The congestus contribution to precipitation is highly sensitive to exactly how congestus clouds are defined.

[52] 3. During both the suppressed and active phases of the ISO, liquid-water profiles and echo-top heights in congestus exhibit a unique signature near the 0° isotherm consistent with cloudy-air detrainment.

[53] 4.In many ways, cumulus congestus act like overgrown trade cumulus.

[54] Although we speak of shallow, congestus, and deep tropical clouds, the vertical distribution of tropical clouds is, in reality, continuous. The congestus mode itself is most prominent when deep convection is absent. It is important, therefore, to not dwell overly on the "modal" aspect of the trimodal distribution: even if no distinct congestus mode is apparent, the presence of tropical congestus is highly likely. The cloud distributions in our simulations appear too trimodal and not as continuous as the distributions in *DeMott and Rutledge* [1998] and *Johnson et al.* [1999], a result we think partially arises from the small domain size to some degree

restricting cloud system variability (i.e., the amount of clouds of different depths that can coexist).

[55] Our desire to resolve small-scale cumulus and congestus clouds with some fidelity yet also employs a domain of sufficient size to represent a degree of mesoscale organization necessitates some caveats. First, as we mentioned in section 2, our choice of horizontal grid spacing is a compromise, as 200 m is overly large to be considered in the realm of true large-eddy simulation (LES), the technique commonly used to study these clouds. Use of this relatively coarse grid spacing means that turbulent cloud fluxes are not as realistic as they could be. Second, the warm-rain microphysical processes in the model are governed by a simple, Kessler-type parameterization, which is known to have limitations for shallow clouds [*Wood*, 2005]. Furthermore, the *Lin et al*. [1983] parameterization used to represent ice-phase processes has long been known to have serious deficiencies when attempting to represent large stratiform regions of MCSs [*McCumber et al*., 1991]. Finally, as mentioned above, the limited domain size is able to capture some but not all aspects of the mesoscale circulation. In particular, the large stratiform regions of mesoscale convective systems during the active phase are probably not well captured.

[56] Future simulations would ideally employ finer grid spacing, a larger domain, and a more sophisticated microphysical parameterization. Assuming a doubling of computational capability, which aspect(s) of the simulation should we improve? The answer depends upon which particular features of the simulation we wish to represent with the most fidelity. Moving to a more sophisticated two-moment microphysical parameterization would entail only a modest increase in computational expense and would better represent both warm-rain and ice-phase microphysical processes. As far as the resolution versus domain size issue, if shallow clouds and congestus are of the greatest concern, increasing the resolution into the realm of true LES would be desirable. If the goal is to explore deep convection in more detail, the domain size should be increased.

[57] This analysis is a based on instantaneous snapshots of the cloud and precipitation field, and we do not follow coherent cloud structures throughout their evolution. *Luo et al*. [2009] found that ~30–40% of tropical congestus fit a "transient" category, meaning a cloud identified as congestus which in reality is growing to eventually become deep cumulonimbus. During the suppressed period of our simulation, when only shallow convection and congestus are present, this issue is not a problem. However, it may be an issue during the active phase when a more complete distribution of cloud depths is present. This problem may be compounded by the possible differences in how much precipitation is produced by a mature cumulus congestus cloud versus a cloud transitioning to its cumulonimbus stage.

[58] One worthy future goal is to evaluate the importance of congestus in the large-scale tropical circulation. Because congestus contributes substantially to surface precipitation, it will have a similarly important diabatic heating signal, though the heating profile will be much shallower than the profile for deep convection. A long-term, unforced, radiative-convective equilibrium numerical modeling framework would be required to assess questions associated with how the large-scale environment influences congestus clouds and how the congestus clouds precondition the tropical environment for deep convective episodes.

[59] **Acknowledgments.** We wish to thank Minghua Zhang for use of his variational analysis of the TOGA COARE observational data. We appreciate the ongoing efforts of Marat Khairoutdinov for making SAM available to the atmospheric science community. We appreciate fruitful discussions with Sue van den Heever, Sandra Yuter, Dick Johnson, Courtney Schumacher, and Yefim Kogan on the topic of congestus clouds. Thanks to Matthew Miller and Sandra Yuter (North Carolina State University) for use of the blob/feature detection toolbox. We greatly appreciate the thoughtful comments from two reviewers and Associate Editor Steve Krueger, who all encouraged us to scrutinize our results in greater depth. This research was supported by the U.S. National Oceanic and Atmospheric Administration (NOAA) Climate Program Office (CPO) Climate Prediction Program for the Americas/Earth System Science Program (CPPA/ESS) grants NA10OAR4310160, the Department of Energy Office of Science grant DE-SC0006736, and the Office of Naval Research award N00014-11-1-0518.

References

Betts, A. K. (1973), Nonprecipitating cumulus convection and its parameterization, *Q. J. R. Meteorol. Soc.*, *99*, 178–196.

Brown, R. G., and C. Zhang (1997), Variability of midtropospheric moisture and its effect on cloud-top height distribution during TOGA COARE, *J. Atmos. Sci.*, *54*, 2760–2774.

Bryan, G. H., J. C. Wyngaard, and J. M. Fritsch (2003), Resolution requirements for the simulation of deep moist convection, *J. Atmos. Sci.*, *131*, 2394–2416.

Carpenter, R. L., Jr., K. K. Droegemeier, and A. M. Blyth (1998a), Entrainment and detrainment in numerically simulated cumulus congestus clouds. Part I: General results, *J. Atmos. Sci.*, *55*, 3417–3432.

Carpenter, R. L., Jr., K. K. Droegemeier, and A. M. Blyth (1998b), Entrainment and detrainment in numerically simulated cumulus congestus clouds. Part II: Cloud budgets, *J. Atmos. Sci.*, *55*, 3433–3439.

Carpenter, R. L., Jr., K. K. Droegemeier, and A. M. Blyth (1998c), Entrainment and detrainment in numerically simulated cumulus congestus clouds. Part III: Parcel analysis, *J. Atmos. Sci.*, *55*, 3440–3455.

Casey, S. P. F., A. E. Dessler, and C. Schumacher (2007), Frequency of tropical precipitating clouds as observed by the Tropical Rainfall Measuring Mission Precipitation Radar and ICESat/Geoscience Laser Altimeter System, *J. Geophys. Res.*, *112*, D14215, doi:10.1029/2007JD008468.

Casey, S. P. F., A. E. Dessler, and C. Schumacher (2009), Five-year climatology of midtroposphere dry air layers in warm tropical ocean regions as viewed by AIRS/Aqua, *J. Appl. Meteorol. Climatol.*, *48*, 1831–1842.

Casey, S. P. F., E. J. Fetzer, and B. H. Kahn (2012), Revised identification of tropical oceanic cumulus congestus as viewed by CloudSat, *Atmos. Chem. Phys.*, *12*, 1587–1595.

Chen, S. S., R. A. Houze, Jr., and B. E. Mapes (1996), Multiscale variability of deep convection in relation to large-scale circulaton in TOGA COARE, *J. Atmos. Sci.*, *53*, 1380–1409.

Cheng, C.- P., and R. A. Houze, Jr. (1979), The distribution of convective and mesoscale precipitation in GATE radar echo patterns, *Mon. Weather Rev.*, *107*, 1370–1381.

Ciesielski, P. E., R. H. Johnson, P. T. Haertel, and J. Wang (2003), Corrected TOGA COARE sounding humidity data: Impact on diagnosed properties of convection and climate over the warm pool, *J. Clim.*, *16*, 2370–2384.

Clothiaux, E. E., K. P. Moran, B. E. Martner, T. P. Ackerman, G. G. Mace, T. Uttal, J. H. Mather, K. B. Widener, M. A. Miller, and D.

J. Rodriguez (1995), The atmospheric radiation measurement program cloud radars: Operational modes, *J. Atmos. Oceanic Technol.*, *12*, 201–229.

Collins, W. D., P. J. Rasch, B. A. Boville, J. J. Hack, J. R. McCaa, D. L. Williamson, and B. P. Briegleb (2006), The formulation and atmospheric simulation of the Community Atmospheric Model version 3 (CAM3), *J. Clim.*, *19*, 2144–2161.

Deardorff, J. W. (1980), Stratocumulus-capped mixed layers derived from a three-dimensional model, *Boundary Layer Meteorol.*, *18*, 495–527.

DeMott, C. A., and S. A. Rutledge (1998), The vertical structure of TOGA COARE convection. Part I: Radar echo distributions, *J. Atmos. Sci.*, *55*, 2730–2747.

Ferrier, B. S. (1994), A double-moment multiple-phase four-class bulk ice scheme. Part I: Description, *J. Atmos. Sci.*, *51*, 249–280.

Haynes, J. M., and G. L. Stephens (2007), Tropical oceanic cloudiness and the incidence of precipitation: Early results from CloudSat, *Geophys. Res. Lett.*, *34*, L09811, doi:10.1029/2007GL029335.

Hollars, S., Q. Fu, J. Comstock, and T. Ackerman (2004), Comparison of cloud-top height retrievals from ground-based 35 GHz MMCR and GMS-5 satellite observations at ARM TWP Manus site, *Atmos. Res.*, *72*, 169–186.

Jensen, M. P., and A. D. Del Genio (2006), Factors limiting convective cloud-top height at the ARM Nauru island climate research facility, *J. Clim.*, *19*, 2105–2117.

Johnson, R. J., P. E. Ciesielski, and K. A. Hart (1996), Tropical inversions near the 0°C level, *J. Atmos. Sci.*, *53*, 1838–1855.

Johnson, R. J., T. M. Rickanbach, S. A. Rutledge, P. E. Ciesielski, and W. H. Schubert (1999), Trimodal characteristics of tropical convection, *J. Clim.*, *12*, 2397–2418.

Khairoutdinov, M. F., and D. A. Randall (2002), Similarity of deep continental cumulus convection as revealed by a three-dimensional cloud-resolving model, *J. Atmos. Sci.*, *59*, 2550–2566.

Khairoutdinov, M. F., and D. A. Randall (2003), Cloud resolving modeling of the ARM summer 1997 IOP: Model formulation, results, uncertainties, and sensitivities, *J. Atmos. Sci.*, *60*, 607–625.

Khairoutdinov, M. F., S. K. Krueger, C.- H. Moeng, P. A. Bogenschultz, and D. A. Randall (2009), Large-eddy simulation of marine deep tropical convection, *J. Adv. Model. Earth Syst.*, *1*, 15, doi:10.3894/JAMES.2009.1.15.

Kogan, Y. L. (1991), The simulation of a convective cloud in a 3-D model with explicit microphysics. Part I: Model description and sensitivity experiments, *J. Atmos. Sci.*, *48*, 1160–1188.

Lasher-Trapp, S. B., C. A. Knight, and J. M. Straka (2001), Early radar echoes from ultragiant aerosol in a cumulus congestus: Modeling and observations, *J. Atmos. Sci.*, *58*, 3545–3562.

Li, C., X. Jia, J. Ling, W. Zhou, and C. Zhang (2009), Sensitivity of MJO simulations to diabatic heating profiles, *Clim. Dyn.*, *32*, 167–187, doi:10.1007/s00382-008-0455-x.

Lin, Y.- L., R. D. Farley, and H. D. Orville (1983), Bulk parameterization of the snow field in a cloud model, *J. Clim. Appl. Meteorol.*, *22*, 1065–1092.

Liu, C., and E. J. Zipser (2009), "Warm rain" in the tropics: Seasonal and regional distributions based on 9 yr of TRMM data, *J. Clim.*, *22*, 767–779.

Luo, Z., G. Y. Liu, G. L. Stephens, and R. H. Johnson (2009), Terminal versus transient cumulus congestus: A CloudSat perspective, *Geophys. Res. Lett.*, *36*, L05808, doi:10.1029/2008GL036927.

Mace, G. G., R. Marchand, Q. Zhang, and G. Stephens (2007), Global hydrometeor occurrence as observed by CloudSat: Initial observations from summer 2006, *Geophys. Res. Lett.*, *34*, L09808, doi:10.1029/2006GL029017.

Madden, R., and P. Julian (1971), Detection of a 40–50 day oscillation in the zonal wind in the tropical pacific, *J. Atmos. Sci.*, *28*, 702–708.

Madden, R., and P. Julian (1972), Description of global scale circulation cells in the tropics with a 40–50-day period, *J. Atmos. Sci.*, *29*, 1109–1123.

Malkus, J. S. (1962), Large-scale interactions, in *The Sea: Ideas and Observations on Progress in the Study of the Seas, 1: Physical Oceanography*, edited by M. Hill, pp. 88–294, Wiley-Interscience, New York.

Malkus, J. S., and H. Riehl (1964), *Cloud Structure and Distributions Over the Tropical Pacific Ocean*, 229 pp., Univ. of Calif. Press, Berkeley, Calif.

Mapes, B. E., and P. Zuidema (1996), Radiative–dynamical consequences of dry tongues in the tropical troposphere, *J. Atmos. Sci.*, *53*, 620–638.

McCumber, M., W.- K. Tao, J. Simpson, R. Penc, and S.- T. Soong (1991), Comparison of ice-phase microphysical parameterization schemes using numerical simulations of tropical convection, *J. Appl. Meteorol.*, *30*, 985–1004.

Mechem, D. B., S. E. Yuter, and S. P. de Szoeke (2012), Thermodynamic and aerosol controls in southeast pacific stratoumulus, *J. Atmos. Sci.*, *69*, 1250–1266.

Miller, M. A., and S. E. Yuter (2013), Detection and characterization of heavy drizzle cells within subtropical marine stratocumulus using AMSR–E 89-GHz passive microwave measurements, *Atmos. Meas. Tech.*, *6*, 1–13, doi:10.5194/amt-6-1-2013.

Rauber, R., H. T. Ochs, III, L. Di Girolamo, S. Göke, and E. Snodgrass (2007), Rain in (shallow) cumulus over the ocean—the RICO campaign, *Bull. Am. Meteorol. Soc.*, *88*, 1912–1928.

Redelsperger, J.- L., D. B. Parsons, and F. Guichard (2002), Recovery processes and factors limiting cloud-top height following the arrival of a dry intrusion observed during TOGA COARE, *J. Atmos. Sci.*, *59*, 2438–2457.

Riehl, H., C. Yeh, J. S. Malkus, and N. E. LaSeur (1951), The northeast trade of the Pacific ocean, *Q. J. R. Meteorol. Soc.*, *77*, 598–626.

Rutledge, S. A., and P. V. Hobbs (1984), The mesoscale and microscale structure and organization of clouds and precipitation in midlatitude cyclones. XII: A diagnostic modeling study of precipitation development in narrow cold-front rainbands, *J. Atmos. Sci.*, *41*, 2949–2972.

Schumacher, C., and R. A. Houze, Jr. (2003), The TRMM precipitation radar's view of shallow, isolated rain, *J. Appl. Meteorol.*, *42*, 1519–1524.

Short, D. A., and K. Nakamura (2008), TRMM radar observations of shallow precipitation over the tropical oceans, *J. Clim.*, *13*, 4107–4124.

Short, D. A., P. A. Kucera, B. S. Ferrier, J. C. Gerlach, S. A. Rutledge, and O. W. Thiele (1997), Shipboard radar rainfall patterns within the TOGA COARE IFA, *Bull. Am. Meteorol. Soc.*, *78*, 2817–2836.

Simpson, J., G. van Helvoirt, and M. McCumber (1982), Three-dimensional simulations of cumulus congestus clouds on GATE day 261, *J. Atmos. Sci.*, *39*, 126–145.

Smolarkiewicz, P. K., and W. W. Grabowski (1990), The multidimensional positive definite advection transport algorithm: Nonoscillatory option, *J. Comput. Phys.*, *86*, 355–375.

Stephens, G. L., and N. B. Wood (2007), Properties of tropical convection observed by millimeter-wave radar systems, *Mon. Weather Rev.*, *135*, 821–842.

Stevens, B. (2007), On the growth of layers of non-precipitating cumulus convection, *J. Atmos. Sci.*, *64*, 2916–2931.

Takemi, T., O. Hirayama, and C. Liu (2004), Factors responsible for the vertical development of tropical oceanic cumulus convection, *Geophys. Res. Lett.*, *31*, L11109, doi:10.1029/2004GL020225.

Tanelli, S., S. L. Durden, E. Im, K. S. Pak, D. G. Reinke, P. Partain, J. M. Haynes, and R. T. Marchand (2008), CloudSat's cloud profiling radar after two years in orbit: Performance, calibration, and processing, *IEEE Trans. Geosci. Remote Sens.*, *46*, 3560–3573.

van den Heever, S., G. L. Stephens, and N. B. Wood (2011), Aerosol indirect effects on tropical convection characteristics under conditions of radiative–convective equilibrium, *J. Atmos. Sci.*, *68*, 699–718.

van Zanten, M. C., B. Stevens, G. Vali, and D. H. Lenschow (2005), Observations of drizzle in nocturnal marine stratocumulus, *J. Atmos. Sci.*, *62*, 88–106.

van Zanten, M. C., et al. (2011), Controls on precipitation and cloudiness in simulations of trade-wind cumulus as observed during RICO, *J. Adv. Model. Earth Syst.*, *3*, M04001, doi:10.1029/2011MS000056.

Waite, M. L., and B. Khouider (2010), The deepening of tropical convection by congestus preconditioning, *J. Atmos. Sci.*, *67*, 2601–2615.

Wang, H., and G. Feingold (2009a), Modeling mesoscale cellular structures and drizzle in marine stratocumulus. Part I: Impact of drizzle on the formation and evolution of open cells, *J. Atmos. Sci.*, *66*, 3237–3256.

Wang, H., and G. Feingold (2009b), Modeling mesoscale cellular structures and drizzle in marine stratocumulus. Part II: The

microphysics and dynamics of the boundary region between open and closed cells, *J. Atmos. Sci.*, *66*, 3257–3275.

Webster, P. J., and R. Lukas (1993), TOGA COARE: The coupled ocean–atmosphere response experiment, *Bull. Am. Meteorol. Soc.*, *73*, 1377–1416.

Wheeler, M. C., and H. H. Hendon (2004), An all-season real-time multivariate MJO index: Development of an index for monitoring and prediction, *Mon. Weather Rev.*, *132*, 1917–1932.

Wood, R. (2005), Drizzle in stratiform boundary layer clouds. Part II: Microphysical aspects, *J. Atmos. Sci.*, *62*, 3034–3050.

Wu, X., W. W. Grabowski, and W. M. Moncrieff (1998), Long-term behavior of cloud systems in TOGA COARE and their interactions with radiative and surface processes. Part I: Two-dimensional modeling study, *J. Atmos. Sci.*, *55*, 2693–2714.

Yoneyama, K., and D. B. Parsons (1999), A proposed mechanism for the intrusion of dry air into the tropical western Pacific region, *J. Atmos. Sci.*, *56*, 1524–1546.

Zeng, X., W.-K. Tao, M. Zhang, A. Y. Hou, S. Xie, S. Lang, X. Li, D. O. Starr, X. Li, and J. Simpson (2009), An indirect effect of ice nuclei on atmospheric radiation, *J. Atmos. Sci.*, *66*, 41–61.

Zhang, M. H., and J. L. Lin (1997), Constrained variational analysis of sounding data based on column-integrated budgets of mass, heat, moisture, and momentum: Approach and application to ARM measurements, *J. Atmos. Sci.*, *54*, 1503–1524.

Zhang, Y., S. Klein, G. G. Mace, and J. Boyle (2007), Cluster analysis of tropical clouds using CloudSat data, *Geophys. Res. Lett.*, *34*, L12813, doi:10.1029/2007GL029336.

Corresponding author: D. B. Mechem, Atmospheric Science Program, Department of Geography, University of Kansas, 1475 Jayhawk Blvd., Lawrence, KS 66045, USA. (dmechem@ku.edu)